Hindawi
Geofluids
Volume 2021, Article ID 6629187, 13 pages
https://doi.org/10.1155/2021/6629187

Research Article

3D Primary Geochemical Halo Modeling and Its Application to the Ore Prediction of the Jiama Polymetallic Deposit, Tibet, China

Zhongping Tao,[1,2] **Bingli Liu**,[1,3] **Ke Guo**,[1] **Na Guo**,[1] **Cheng Li**,[1] **Yao Xia**,[4] **and Yaohua Luo**[1]

[1]*Geomathematics Key Laboratory of Sichuan Province (Chengdu University of Technology), Chengdu 610059, China*
[2]*Information Technology Center, Chengdu Sport Institute, Chengdu 610041, China*
[3]*Key Laboratory of Geochemical Exploration, Institute of Geophysical and Geochemical Exploration, CAGS, Langfang, Hebei 065000, China*
[4]*China Institute of Geo-Environment Monitoring, Beijing 100081, China*

Correspondence should be addressed to Bingli Liu; liubingli-82@163.com

Received 28 December 2020; Revised 3 May 2021; Accepted 29 July 2021; Published 20 August 2021

Academic Editor: Mercè Corbella

The identification of primary geochemical haloes can be used to predict mineral resources in deep-seated orebodies through the delineation of element distributions. The Jiama deposits a typical skarn–porphyry Cu–polymetallic deposit in the Gangdese metallogenic belt of Tibet. The Cu–polymetallic skarn, Cu–Mo hornfels, and Mo ± Cu porphyry mineralization there exhibit superimposed geochemical haloes at depth. Three-dimensional (3D) primary geochemical halo modeling was undertaken for the deposit with the aim of providing geochemical data to describe element distributions in 3D space. An overall geochemical zonation of Zn(Pb) → Au → Cu(Ag) → Mo gained from geochemical cross-sections, together with dip-direction skarn zonation Pb–Zn(Cu) → Cu(Au–Ag–Mo) → Mo(Cu) → Cu–Mo(Au–Ag) and vertical zonation Cu–(Pb–Zn) → Mo–(Cu) → Mo–Cu–(Ag–Au–Pb–Zn) → Mo in the #24 exploration profile, indicates potential mineralization at depth. Integrated geochemical anomalies were extracted by kernel principal component analysis, which has the advantage of accommodating nonlinear data. A maximum-entropy model was constructed for deep mineral resources of uncertainty prediction. Three potential deep mineral targets are proposed on the basis of the obtained geochemical information and background.

1. Introduction

Primary geochemical halo identification is a key approach for detecting mineral deposits near or below the ground surface [1]. A primary geochemical halo is an area of rocks surrounding mineral deposits (orebodies) enriched in ore-forming elements [2]. Primary geochemical characteristics of mineral deposits provide important information for predicting deep mineral resources, as they reflect the geochemical processes of metal precipitation and mineral formation. Many methods have been used to identify primary halo characteristics of mineral deposits, including vertical element zonation [3–5], element ratios vectoring toward ore zones [6–8], Pearce element ratios [1, 9–12], and alteration indices [13–21]. A major aspect of these methods is the determination of spatial distributions of single elements and/or element associations.

Within the Jiama Cu–polymetallic deposit in Tibet, previous studies focused on element zonation based on lithogeochemical data for surface samples and those from orebodies to build an exploration model for deep mineral resources [22–29]. Primary geochemical zonation and elemental distributions have thus been proved to be valid methods for estimating mineral resources at Jiama. Three-dimensional (3D) modeling is also an efficient approach that has been widely applied in deep mineral exploration [30–33], with 3D visualizations of primary geochemical haloes directly reflecting the spatial distribution of elements [34, 35]. A 3D model of primary haloes can be useful in geochemical studies of mineral

deposits because it provides insights into mineralization systems, with important implications for exploration. In this study, 3D halo modeling was undertaken to extend geochemical zonation to stereoscopic space to provide more information on deep mineral resources.

Lithogeochemical data from sources such as drill cores usually have nonlinear features that require processing by nonlinear algorithms. Kernel principal component analysis (KPCA) has been identified as a useful method for extracting integrated information from multielement drill-core data [36, 37]. KPCA is a type of nonlinear PCA developed by extension of the kernel method [38] and involves the transfer of original inputs to a high-dimensional feature space by the kernel method with PCA of that space [39]. KPCA has been used in remote-sensing image classification [36, 37], multidimensional space uncertainty modeling [40], anomaly detection in hyperspectral imagery [41], and volcanic reservoir fracture discrimination [42].

Machine learning (ML) has provided a new means of building models based on large data volumes [43–45]. ML algorithms that consider relationships between prediction and response variables through direct modeling have proved effective in capturing complex nonlinear relationships between geochemical models and mineralization [44, 46], including the use of logic regression [43], neural networks [47], support vector machine [45], random forest [48], and maximum-entropy (MaxEnt) model [49, 50]. A MaxEnt model is a high-performance statistical model often used in probabilistic estimation. It is suitable for classification problems and shows a performance superior to that of other methods, especially with limited sample data [51, 52]. MaxEnt modeling has been widely applied in such fields as natural language processing [53, 54], economic prediction [55], the geographical distribution of animal and plant species [56], and mineral resource prediction [49, 50].

In this study, lithogeochemical data from drill cores were used to build a 3D primary geochemical halo model through spatial interpolation, aiming to describe element distributions at depth in the Jiama deposit. The cutting of cross-sections and vertical profiles was applied to investigate spatial variations in different elements, and the KPCA method was used to produce profile integrated geochemical information, with MaxEnt modeling being applied to predict exploration targets.

2. Materials and Methods

2.1. Geological Setting. The Jiama deposit is one of the most economically significant Cu deposits in Tibet and lies in the Gangdese metallogenic belt within the eastern Tethyan metallogenic domain [24, 28, 29, 57] (Figure 1). Collision of the India–Asia plates during the Paleocene and ensuing post-collisional magmatism during the Miocene caused the formation of the Gangdese belt, which hosts several giant porphyry Cu deposits [57–62] and is highly prospective for Cu–polymetallic deposits, containing >18 Mt of Cu resources [35, 59]. Proven resources of the Jiama deposit include 7.4 Mt Cu, 0.6 Mt Mo, 1.8 Mt (Pb + Zn), 6.65 Moz Au, and 360.32 Moz Ag [23].

Jiama stratigraphy comprises Upper Jurassic Duodigou Formation (J_3d) limestone and marble and overlying Lower Cretaceous Linbuzong Formation (K_1l) sandstone, siltstone, and shale. Intrusive rocks cropping out in and around the deposit include granite porphyry, granodiorite porphyry, quartz–albitite porphyry, and fine-grained granite. Plutonic rocks (in drill holes) are dikes intruding hornfels and include dolerite, quartz diorite porphyry, granodiorite porphyry, monzonite to quartz monzonitic porphyry, and monzonitic granite porphyry [22, 25, 27, 28, 35, 57, 63–65] (Figure 1).

Geological structures at Jiama are controlled by collision of the India and Eurasia plates and constitute E-trending strike-slip faults and related secondary NW-trending thrusts, including a major thrust nappe structure associated with a series of overturned folds and a gliding nappe covering ~4 km^2. These structures contributed to the formation of the Jiama Cu–polymetallic system [23, 63, 66].

Thermal and hydrothermal alteration has occurred in the Jiama deposit, with the former generating hornfels and marble [67] and the latter being related to porphyry and skarn alteration. Porphyry alteration (with porphyry as the center) changed from the proximal potassic zone (hydrothermal biotite + quartz + K-feldspar) to the middle phyllic zone (quartz + sericite + phengite) and then the peripheral propylitic zone (chlorite + epidote + calcite + quartz). Skarn alteration includes endoskarn and exoskarn, with the former occurring mainly as epidote alteration and the latter including garnet–pyroxene and wollastonite skarn [22, 23, 28, 63].

On the basis of its different host rocks, the Jiama orebody can be divided into Cu–polymetallic skarn (orebodiesI and II), Cu–Mo hornfels (orebody III), and Mo ± Cu porphyry mineralization (orebody IV) [23]. Skarn orebody is regard as the most important orebody type at present as it constitutes over 70% of the reserves. In addition, porphyry orebody has raised much attention for its high mineral prospectivity [22, 28, 35, 57].

2.2. Data. The dataset included 71,434 samples from 381 drill holes and 10 trenches, collected by the Huatailong Mining Industry Development Co. Ltd., Tibet. The average drill-hole spacing was 100 m, with sampling elevation of 3800–5400 m and drill-core sample lengths of 0.8–3 m. The average trench spacing was 100 m, with depths of 10–25 m and lengths of 6.6–66.4 m. The elements analyzed were Au, Ag, Cu, Mo, Pb, and Zn, with sample preparation, analysis, and quality control methods following Chinese Geochemical Survey Specifications DZ0130−94.

2.3. KPCA. KPCA was originally developed by Scholkopf et al. [38] and is aimed at converting original nonlinear inputs into a high-dimensional feature space through the kernel method, with PCA applied to this space [39]. Details of the fundamental theory of the method have been given by Scholkopf et al. [38, 68]. Extraction of geochemical integrated information by KPCA follows the steps given below.

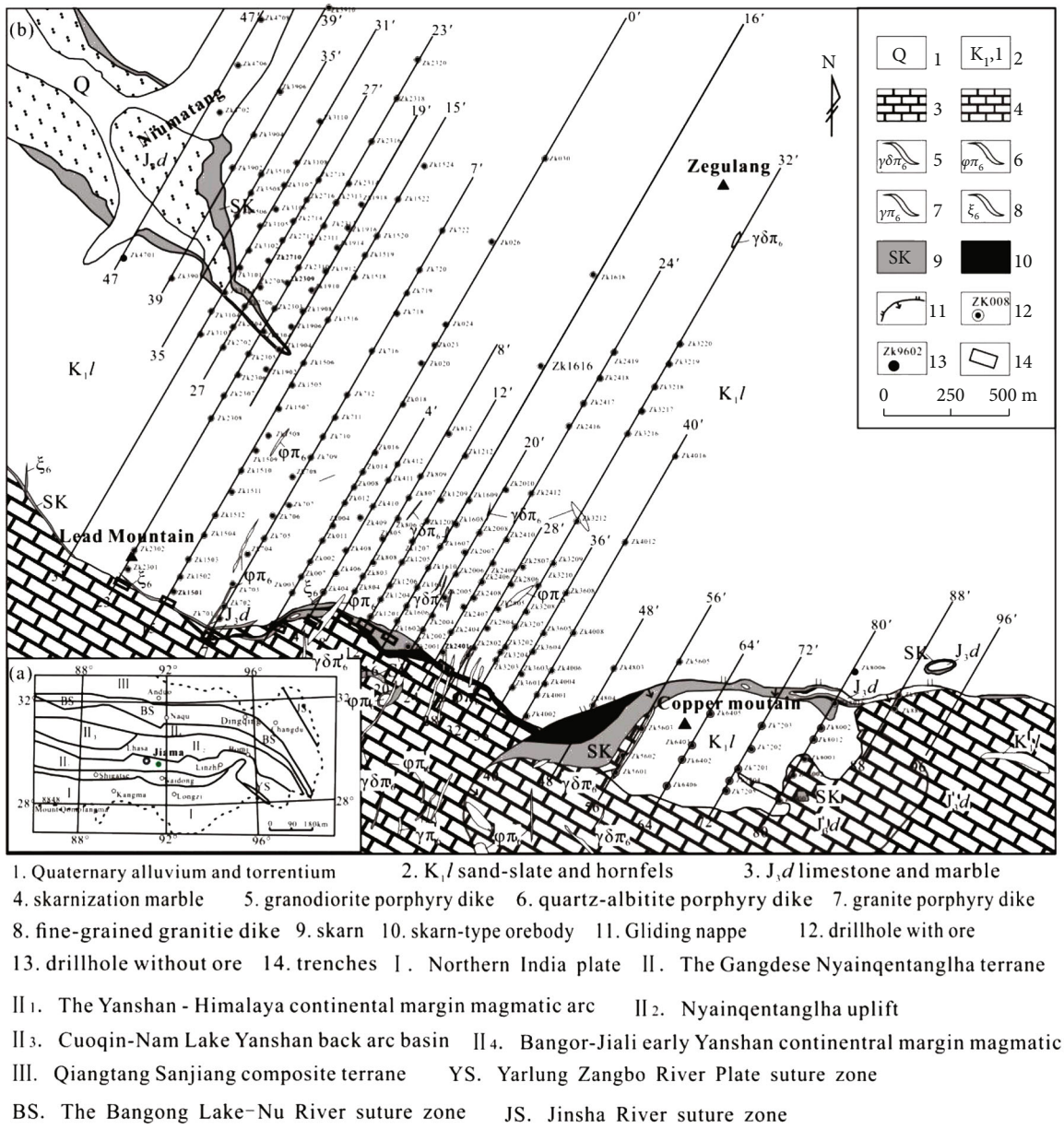

Figure 1: Geological maps of (a) the geo-tectonic background of the region surrounding Jiama and (b) the Jiama polymetallic deposit (modified from [23, 28, 29, 57]).

The lithogeochemical sample-data input dataset can be described as matrix A_{mn}comprising n elements and m samples:

$$A_{mn} = \begin{pmatrix} a_{11} & \cdots & a_{1n} \\ \vdots & \ddots & \vdots \\ a_{m1} & \cdots & a_{mn} \end{pmatrix}. \quad (1)$$

(1) The Gaussian kernel (a classic kernel; [69]) is used to calculate the kernel matrix,K:

$$K(x_i, x_j) = \exp\left(-\frac{\|x - x_i\|^2}{\sigma^2}\right) \sigma \in R^+. \quad (2)$$

(2) Eigenvalues $\lambda_1, \cdots, \lambda_n$ of the kernel matrix and corresponding eigenvectors,$v_1, \cdots, v_n$, are calculated

(3) Descending-order eigenvalues provide the eigenvectors $v'_1, \cdots, v'_n$

(4) Centralization and orthogonalization to the eigenvectors $v'_1, \cdots, v'_n$ gives the feature vectors,$\alpha_1, \cdots, \alpha_n$

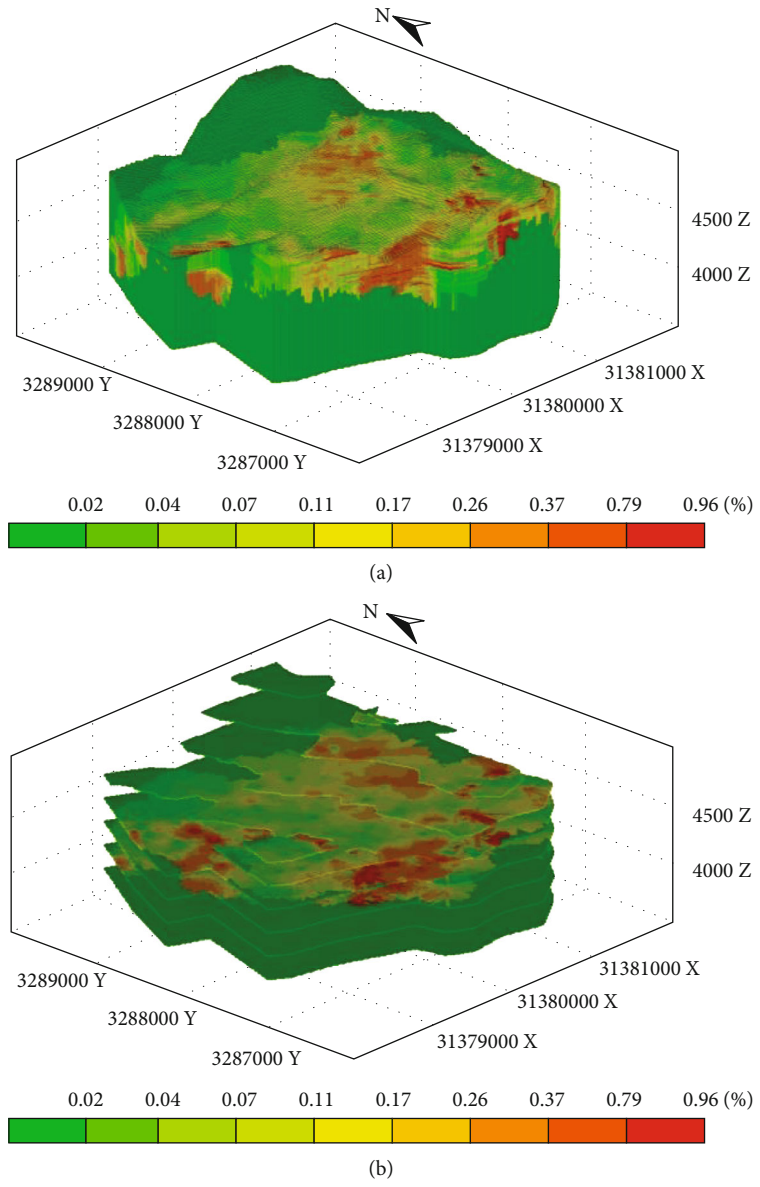

Figure 2: 3D model of (a) the primary geochemical halo of Cu and (b) its cross-section cuttings in the Jiama deposit.

(5) Calculation of the projection of K by $Y = KL \times \alpha$ where L is the eigenvalue matrix and Y is the integrated geochemical information extraction by KPCA

2.4. MaxEnt Model. The concept of information entropy was first introduced by Shannon [70] and represents the expected value of information contained in messages [71]. As a measure of the uncertainty of random events, the information entropy can be expressed as

$$H(p) = -\sum_{i=1}^{n} p_i \log(p_i), \quad (3)$$

where $H(p)$ represents the information entropy and p_i is the probability of the ith random event. The probability distribution that best represents the current state of knowledge has the highest entropy, based on the MaxEnt principle [72]. The MaxEnt model is constructed according to this principle, together with a log–linear ML-based model. This model can set constraints flexibly and has been successfully applied in mineral resource prediction [49, 50].

3. Results

3.1. 3D Primary Geochemical Halo Modeling of the Jiama Deposit

3.1.1. 3D Primary Geochemical Halo Modeling. Geochemical halo modeling is aimed at building a 3D dataset of primary geochemical haloes to allow visualization of elemental spatial distributions. Elemental content is considered at a particular position with geochemical data varying stereoscopically around it in all directions, rather than involving interpolation

Table 1: Normalized areal metal productivities at different levels.

Elevation	Cu	Ag	Au	Mo	Pb	Zn
5250 m	0.0521	0.0269	0.0414	0.0398	0.0087	0.0141
5050 m	0.1487	0.1185	0.0587	0.0864	0.2665	0.1972
4850 m	0.1213	0.0888	0.0537	0.1052	0.3074	0.3583
4650 m	0.0966	0.0878	0.0670	0.1172	0.2061	0.1316
4450 m	0.2021	0.2376	0.3114	0.1930	0.0885	0.0927
4250 m	0.2083	0.2603	0.2878	0.2192	0.0708	0.1126
4050 m	0.1292	0.1278	0.1130	0.2231	0.0230	0.0514

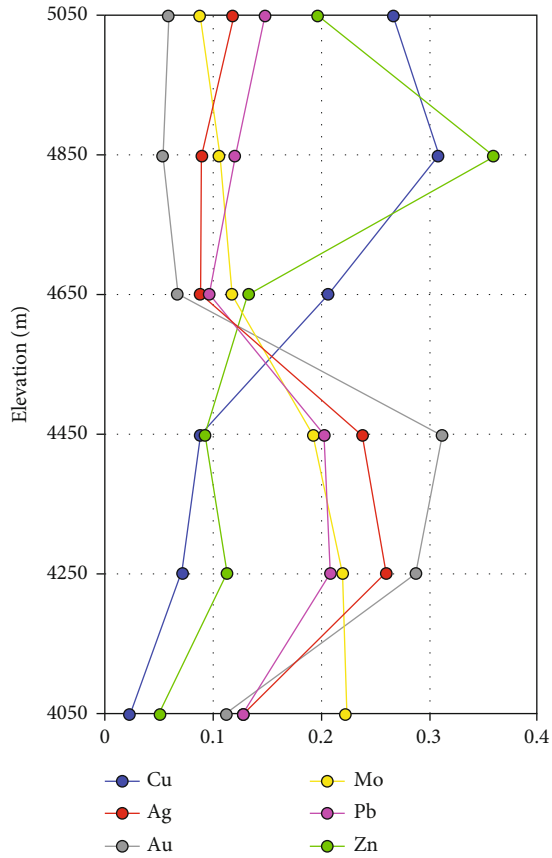

Figure 3: Elevation versus elemental relative abundance.

within a fixed section. In the case of the Jiama deposit data, the modeling involved the following steps.

(1) Designing a spatial range with 1148 m length N–S, 920 m width E–W, and 1735.15 m height, encompassing the entire mineral deposit area

(2) Setting sampling blocks of 20 m × 20 m × 20 m cubes within this spatial range, totaling 2,134,788 cubes

(3) Assigning elemental data to corresponding cubes

(4) Considering the 3D configuration of orebodies including strike, dip direction, and dip angle to build a 3D interpolation ellipsoid, with the search direction set by the strike of orebodies, and the search radius determined by sampling distribution and interval

(5) Interpolating values into unsampled cubes using the inverse distance weighting (IDW) algorithm [73] based on the search ellipsoid

(6) Using different colors to highlight changes in primary geochemical haloes (Figure 2)

3.1.2. Primary Halo Cross-Sections and Its Geochemical Zonation. Areal metal productivities in each potential area of mineralization can be estimated by section cutting based on the 3D primary geochemical halo model.

Analysis of the top-to-bottom distribution of elements involved 200 m equidistant cross-sections over an altitude range of 4050–5250 m (Figure 2(b)). The areal metal productivity for each element in each layer was calculated. The normalized areal metal productivities were used to compare

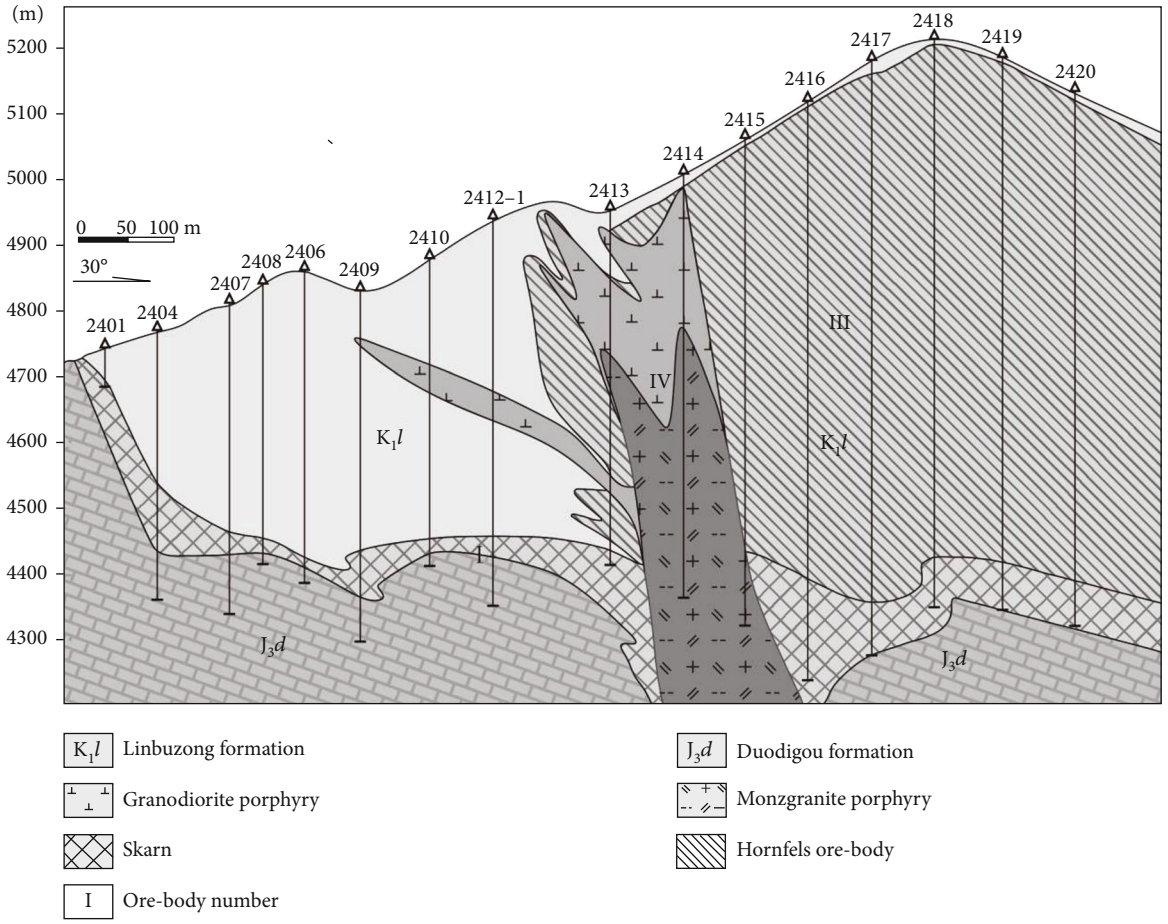

Figure 4: The #24 geological profile of the Jiama deposit (modified from [23, 24]).

element enrichments at different depths (Figure 2 and Table 1).

Sequences of primary haloes indicate elemental zonation in the deposit, as determined by comparison of elemental distributions.

The data presented in Figure 3 and Table 1 indicate a systematic vertical zonation pattern of Zn(Pb) → Au → -Cu(Ag) → Mo from surface to depth in the Jiama deposit. This zonation pattern also indicates two distinct parts of the deposit either side of ~4650 m elevation, with Pb and Zn concentrated above and Au, Ag, Cu, and Mo below. This is consistent with the observed spatial distribution of different types of mineralization (Figure 4).

3.2. Mineral Prediction at Depth

3.2.1. Elemental Distributions in the Profile. The interpolation of values within 3D space provides a more reasonable value than interpolating over a profile. Furthermore, a profile of interest can be cut to investigate the distribution of elements in a certain region. Here, the #24 exploration profile is considered as an example, with a vertical data profile being cut to study elemental distributions.

The #24 exploration profile is typical one of the Jiama deposit as it contains all the orebody types, with hornfels mineralization in its upper part (4300–5200 m elevation); porphyry mineralization below 5000 m elevation as a cone shape amid the hornfels orebody; and skarn mineralization at the contact between porphyry and marble, and in the interlayer detachment zone between Linbuzong Formation hornfels and Duodigou Formation marble. The skarn orebody occurs in lamellar form or as thick plates and is found mainly at elevations of 4000–5000 m [23, 24] (Figure 4).

A total of 7423 pieces of data were obtained from the profile cutting, with results indicating typical nonlinear features with high skewness, kurtosis, and coefficients of variation (Table 2).

In the #24 exploration profile, hornfels and porphyry mineralization occur at elevations of > ~4700 m, spatially consistent with the upper orebodies III and IV, respectively. Skarn mineralization at 4200–4700 m corresponds to orebody I. Molybdenite mineralization below 4700 m includes skarn, hornfels, and porphyry mineralization, which are related to orebodiesI, III, and IV, respectively. Lead and Zn mineralization occurs within Cu mineralization, mainly in the upper skarn orebody I. Au and Ag are hosted mainly within Cu mineralization as by-products of Cu extraction in the skarn orebody I [22–24, 27–29] (Figures 4 and 5).

The geochemical profiles of Cu, Mo, Pb, Zn, Au, and Ag are shown in Figure 5. In skarn, the Cu grade is generally >1% and the Mo grade 0.08%–0.15%, compared with 0.15%–0.4% and ~0.05%, respectively, in porphyry. There is

Table 2: Statistical numerical distribution parameters for the #24 exploration profile (SD: standard deviation; CV: coefficient of variation).

	Cu (%)	Ag (g/t)	Au (g/t)	Mo (%)	Pb (%)	Zn (%)
Mean	0.25	3.14	0.06	0.03	0.02	0.02
Median	0.19	1.06	0.03	0.02	0.0001	0.01
SD	0.36	7.26	0.35	0.03	0.08	0.05
Kurtosis	982.1	721.59	1595.7	22.33	584.9	956.6
Skewness	26.54	21.59	37.67	2.94	19.55	26.46
Minimum	0.01	0.46	0	0	0	0
Maximum	16.21	302.83	17.79	0.43	3.37	2.36
CV	1.446	2.311	5.457	0.921	4.381	3.365

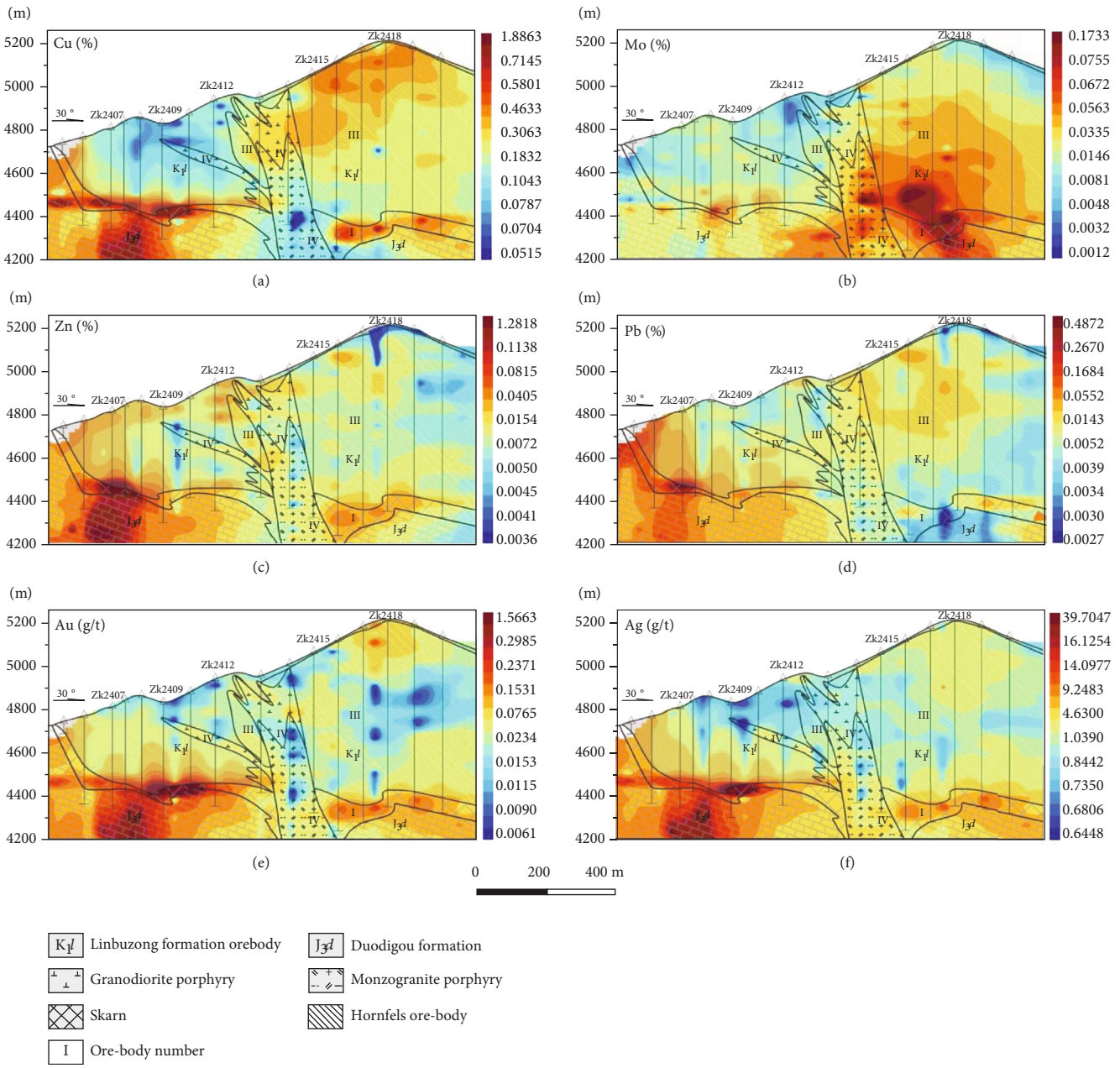

Figure 5: Distributions of different elements in the #24 exploration profile.

Table 3: Normalized linear metal productivities at different elevations.

	Cu	Ag	Au	Mo	Pb	Zn
5150 m	0.118302	0.052047	0.095314	0.013156	0.029841	0.037884
5050 m	0.112563	0.050876	0.071186	0.024542	0.048724	0.046239
4950 m	0.114106	0.054056	0.042499	0.033158	0.083269	0.083759
4850 m	0.084857	0.049415	0.039516	0.044863	0.076262	0.08756
4750 m	0.082904	0.042812	0.031637	0.104643	0.069689	0.077148
4650 m	0.098615	0.04874	0.065079	0.089729	0.057122	0.0603
4550 m	0.059823	0.045364	0.047652	0.097557	0.07686	0.070141
4450 m	0.065125	0.078542	0.063225	0.129823	0.096916	0.099025
4350 m	0.075965	0.165661	0.160413	0.126215	0.113091	0.10536
4250 m	0.085481	0.196438	0.195658	0.117067	0.1299	0.139239
4150 m	0.070164	0.16103	0.146513	0.104968	0.155222	0.103943
4050 m	0.032097	0.055019	0.041309	0.114279	0.063105	0.089402

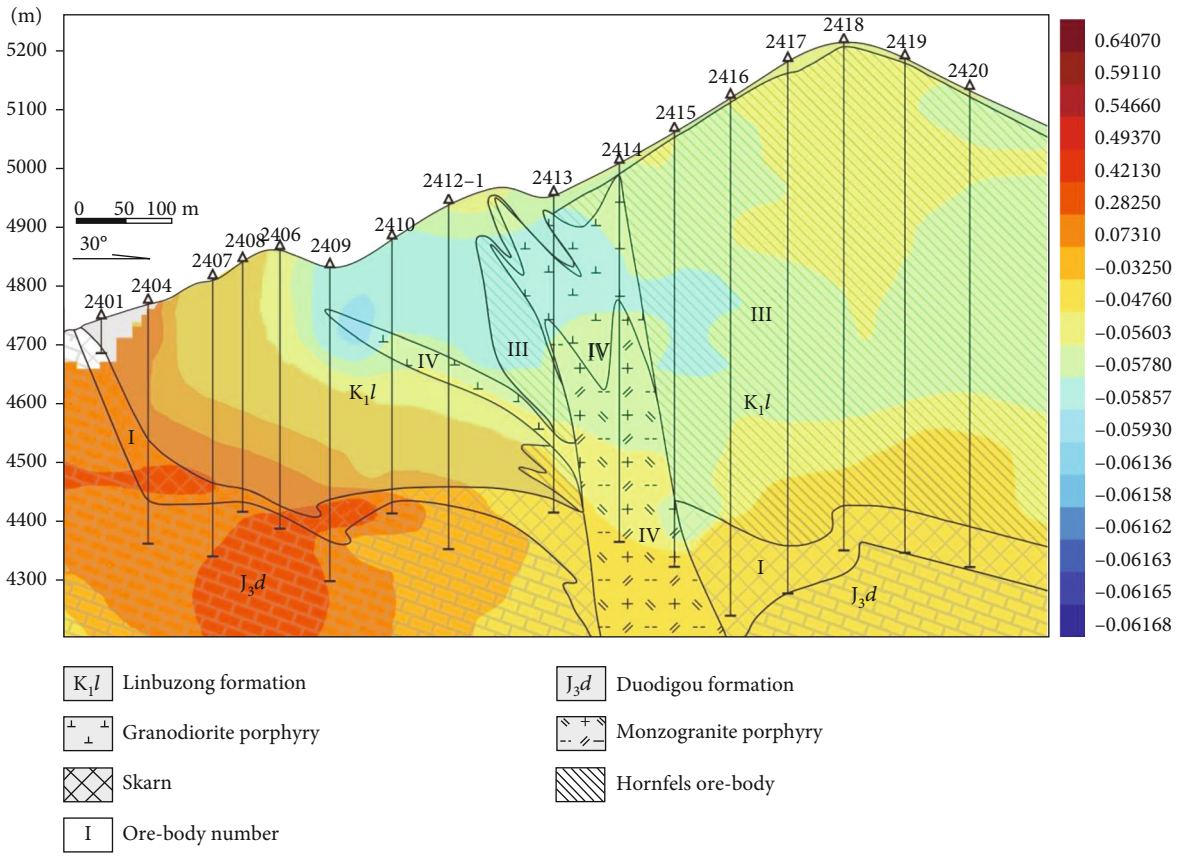

Figure 6: Results of integrated geochemical mapping using KPCA.

a much higher mineralization intensity in skarn, which causes the Cu and Mo anomalies to be concealed in porphyry. Especially, the left part below skarn orebody I has high-grade Cu-Zn-Au-Ag mineralization, in which the drill holes in the #24 exploration profile did not reach. This anomaly is deduced from 3D interpolation, using data from the drill holes next to #24 exploration profiles. In such circumstances, geochemical zonation may be helpful in metal mineralization studies.

In skarn Cu–polymetallic orebody I, Pb and Zn are concentrated mainly in the upper left of the profile, Au and Ag along the orebody dip direction, and Mo in the distal part of dip direction (Figure 5). The Cu content is lower where skarn orebody I and porphyry orebody IV intersect. The sequence Pb–Zn(Cu) → Cu(Au–Ag–Mo) → Mo(Cu) → Cu–Mo(Au–Ag) thus applies to the skarn orebody (Figure 5).

Hornfels and porphyry orebodies III and IV clearly discriminate the upper Cu and lower Mo at an elevation of

~4750 m, consistent with the trends in Cu and Mo mineralization. Overall, the geochemical map and linear metal productivities in the #24 profile (Table 3) indicate elemental zonation of Cu(Pb–Zn) → Mo(Cu) → Mo–Cu(Ag–Au–Pb–Zn) → Mo from top to bottom. Linear productivity reflects the geochemical anomaly at a particular elevation and was calculated using

$$P = \sum_{i=1}^{n} (C_{ai} - C_b) \times d_i, \quad (4)$$

where P is linear productivity, C_{ai} is the value of the geochemical anomaly at aparticular location, d_i is the length where C_{ai} occurs (20 m here), C_b is the value of the geochemical background, and n is the number of samples at the corresponding elevation.

3.2.2. Integrated Distribution in the #24 Exploration Profile. Taking into account the nonlinear characteristics of the primary geochemical halo data (Table 2), the KPCA method was used to extract integrated multielement information for the #24 profile, with principal component 1 explaining 43.46% of the total variance of the kernel-transformed data (Figure 6).

Figure 6 highlights the two parts of the #24 profile, one with the upper of hornfels orebody above ~4700 m and the other around the skarn orebody. The upper unit is characterized by Cu mineralization in hornfels above 4700 m, and the lower unit is associated with Cu–polymetallic mineralization in skarn.

3.2.3. Deep Mineral Resource Prediction for the #24 Profile. The zonation of 3D primary geochemical haloes obtained from cross-section cutting (Section 3.1.2), Zn(Pb) → Au → Cu(Ag) → Mo, is typical of elemental zonation in porphyry Cu mineralization systems, consistent with earlier findings [35, 74], and may be useful for predicting element distributions at greater depth.

The zonation along the skarn orebody reflects Pb–Zn(Cu) → Cu(Au–Ag–Mo) → Mo(Cu) → Cu–Mo(Au–Ag) from upper left to bottom (Figure 5), consistent with the distribution of associated elements around the porphyry intrusions. The skarn orebody I formed in the interlayer detachment zone between the Linbuzong and Duodigou formations and is confined to the contact between porphyry and marble. It dips NE and is ~3000 m long, with a tendency to extended mineralization [23, 24] (Figures 4–6). Moreover, the zonation along the skarn orebody is incomplete and should include an association of Cu–Au–Ag or Cu–Pb–Zn, indicating potential Cu–polymetallic mineralization.

The zonation of element associations from top to bottom of the #24 exploration profile, Cu(Pb–Zn) → Mo(Cu) → Mo–Cu(Ag–Au–Pb–Zn) → Mo, is affected by the different mineralization types. The Cu(Pb–Zn) association is derived from the skarn orebody at an elevation of ~4750 m, the Mo(Cu) association involves the hornfels orebody at ~4650 m, the Mo–Cu(Ag–Au–Pb–Zn) association reflects the composition of the skarn orebody at ~4400 m, and the Mo anomaly at the bottom may indicate deep porphyry molybdenite mineralization. This is especially the case for the profile across the center of the porphyry and hornfels orebodies, where zonation may be an important indicator of deep mineral resources.

Table 4: MaxEnt parameters used in the Jiamacase study.

Parameter	Value
Random test percentage	25%
Regularization multiplier	2.5
Max. number of background points	10000
Maximum iterations	500
Convergence threshold	0.00001
Default prevalence	0.5
Output format	Logistic

The MaxEnt model was applied to the analysis of uncertainties in mineral resource prediction based on elemental distribution (Figure 5), integrated anomalies (Figure 6), and the locations of orebodies. The MaxEnt software was used to establish a prediction model for prospective mineral resource areas (MaxEnt 3.3.3k; http://biodiversityinformatics.amnh.org/open_source/maxent/), with model parameters as given in Table 4. In this simulation, 75% of the data were randomly selected as ML training data and the remaining 25% as test data. The MaxEnt software performed 20 replicated simulations on the optimal model to provide the average value of the model evaluation with the test AUC (Area Under Curve) = 0.929 (Figure 7), which indicates that the model was able to successfully associate the probability of multivariate geochemical anomalies with mineralizations. As shown in Figure 8, mineralizations in #24 profile are spatially consistent with the high anomaly probability zone (red), which could be used as evidence in predicting the location of concealed orebodies with consideration of uncertainty.

The above analysis, in combination with geochemical mapping and geological background (Figures 5 and 6), yielded three prediction targets, namely, 24-1, 24-2, and 24-3 (Figure 8), as discussed below.

4. Discussion

Target 24-1 lies below borehole ZK2409 at an elevation of ~4250 m and is indicated by both multielement anomalies and an integrated KPCA anomaly (Table 1; Figures 5 and 6). The MaxEnt model indicates that this target has a high probability of containing mineral resources and warrants further investigation, as it may be related to a deep porphyry edge or second concealed skarn layer (Figure 8).

Target 24-2 lies under porphyry orebody IV, where a high-Mo anomaly is evident with increasing Mo concentration with depth (Figure 5 and Table 1). The geochemical zonation from top to bottom of the #24 exploration profile, Cu(Pb–Zn) → Mo(Cu) → Mo–Cu(Ag–Au–Pb–Zn) → Mo, provides strong support for this target. From a geological perspective, the extensive deep porphyry suggests a significant prediction direction for as-yet-unidentified porphyry Mo(Cu) mineralizations. A high probability of mineralization that shows in Figure 8 provides the reference of mineral location.

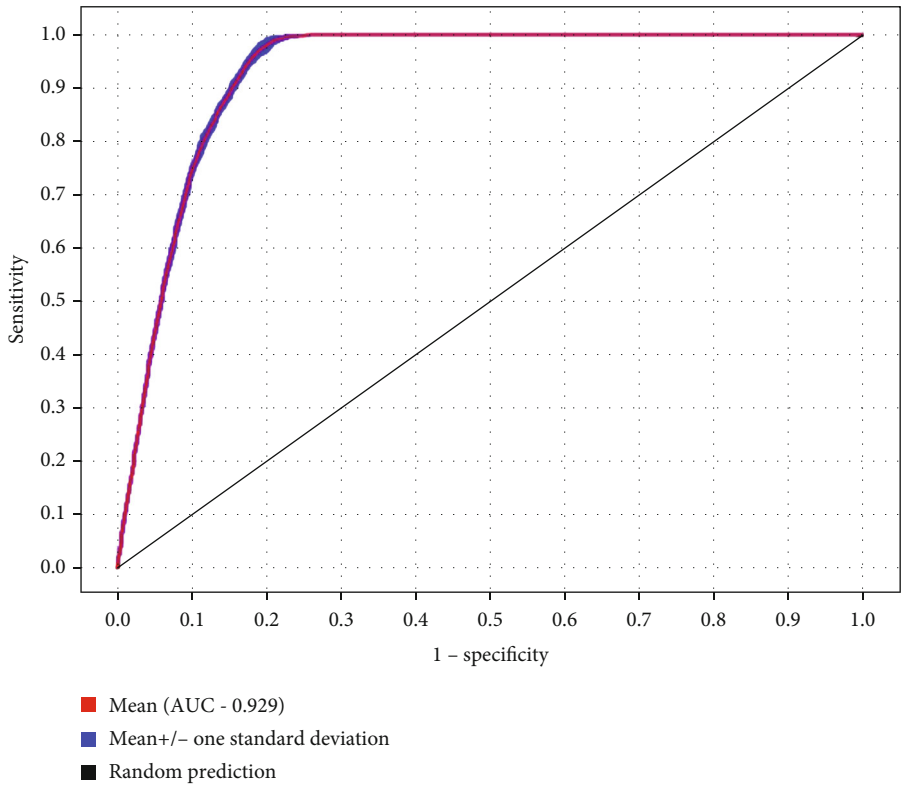

Figure 7: Average test AUC of the MaxEnt model with 20 repetitions.

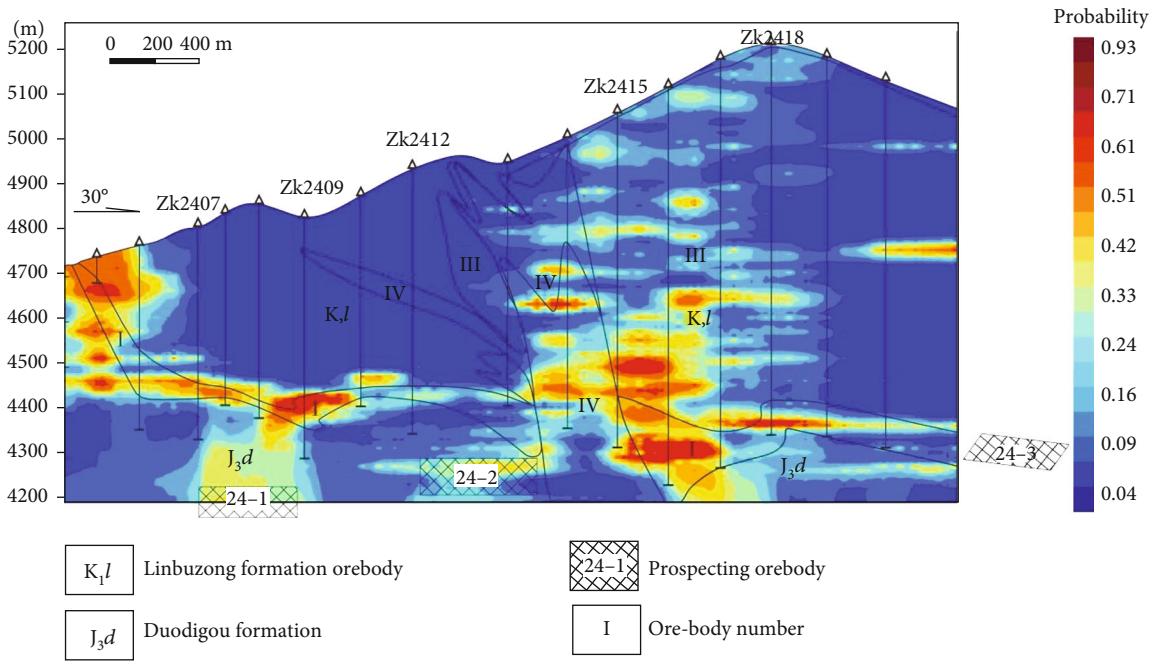

Figure 8: Predicted exploration targets for the #24 profile.

Target 24-3 lies in the northeastern extension of the skarn orebody I, according to zonation along the skarn orebody I and the distribution of skarn. In the geological point, there should be a tendency to skarn dip direction (Figure 4). In the geochemical point, the geochemical zonation, Pb–Zn(Cu) → Cu(Au–Ag–Mo) → Mo(Cu) → Cu–Mo(Au–Ag), indicates a Cu–polymetallic mineralization (Figure 8).

Especially, the overall geochemical vertical zonation of Zn(Pb) → Au → Cu(Ag) → Mo from surface to depth is a typical geochemical pattern of porphyry mineralization,

providing a strong support for the targets above. The MaxEnt model can evaluate the uncertainty of the predicted targets of 24-1 and 24-2, which is also a quantitative evidence for mineralization (Figure 8).

5. Conclusions

(1) In this study, 3D primary geochemical halo modeling was used to build a geochemical data volume by 3D spatial interpolation. In this approach, information was obtained from all directions in 3D space, which is an improvement over interpolation on a fixed surface

(2) Three different geochemical zonations were indicated by the primary geochemical haloes. The cross-section cutting indicated an overall zonation of Zn(Pb) → Au → Cu(Ag) → Mo, reflecting differences in element concentrations from top to bottom, consistent with earlier findings [35, 74]. The profile cutting indicates two different zonations in the #24 profile: one along the dip direction of skarn from surface to depth (Pb–Zn(Cu) → Cu(Au–Ag–Mo) → Mo(Cu) → Cu–Mo(Au–Ag)) indicating skarn orebody extension, and the other (Cu(Pb–Zn) → Mo(Cu) → Mo–Cu(Ag–Au–Pb–Zn) → Mo) gained from linear metal productivities from top to bottom indicating deep porphyry molybdenite mineralization

(3) During the analysis process, an integrated geochemical map was generated by KPCA, and a MaxEnt model was built by combining six single-element geochemical anomalies and an integrated geochemical anomaly for deep mineral resource uncertainty prediction. Finally, three deep-seated mineral targets were identified by the geological and geochemical information extracted from the 3D primary geochemical halo modeling

Data Availability

The data used to support the findings of this study were supplied by Huatailong mining industry development Co., Ltd. and so cannot be made freely available. Requests for access to these data should be made to Huatailong mining industry development Co., Ltd.

Conflicts of Interest

The authors declare no conflicts of interest.

Authors' Contributions

Z.T., B.L., and K.G. contributed to the ideas. B.L. and Z.T contributed to the methodology. Z.T., B.L., C.L., Y.X., and Y.L. contributed to the writing for the original draft preparation. B.L. contributed to the writing involving review and editing. N.G. and C.L. contributed to the modeling. K.G. contributed to the supervision. All authors read and agreed to the published version of the manuscript.

Acknowledgments

We are grateful to the Huatailong Mining Industry Development Co. Ltd. for their support. This research was supported by the National Key R&D Program of China (2016YFC0600604), the Chinese National Natural Science Foundation (41602334 and 41672325), the fund from the Key Laboratory of Geochemical Exploration, Ministry of Natural Resources (AS2019P02-01), and the Opening Fund of Geomathematics Key Laboratory of Sichuan Province (scsxdz2018zd03 and scsxdz2020yb06).

References

[1] E. J. M. Carranza and M. Sadeghi, "Primary geochemical characteristics of mineral deposits – implications for exploration," *Ore Geology Reviews*, vol. 45, pp. 1–4, 2012.

[2] N. I. Safronov, "Dispersion haloes of ore deposits and their use in exploration," *Problemy Sovetskoy Geologii*, vol. 4, pp. 41–53, 1936.

[3] V. V. Distler, M. A. Yudovskaya, G. L. Mitrofanov, V. Y. Prokof'Ev, and E. N. Lishnevskii, "Geology, composition, and genesis of the Sukhoi Log noble metals deposit, Russia," *Ore Geology Reviews*, vol. 24, no. 1-2, pp. 7–44, 2004.

[4] G. M. Gundobin, "Peculiarities in the zoning of primary halos," *Journal of Geochemical Exploration*, vol. 21, no. 1-3, pp. 193–200, 1984.

[5] M. Ziaii, E. J. M. Carranza, and M. Ziaei, "Application of geochemical zonality coefficients in mineral prospectivity mapping," *Computational Geosciences*, vol. 37, no. 12, pp. 1935–1945, 2011.

[6] P. C. Goodell and U. Petersen, "Julcani mining district, Peru: a study of metal ratios," *Economic Geology*, vol. 69, no. 3, pp. 347–361, 1974.

[7] B. K. Jones, "Application of metal zoning to gold exploration in porphyry copper systems," *Journal of Geochemical Exploration*, vol. 43, no. 2, pp. 127–155, 1992.

[8] F. Pirajno and R. H. Smithies, "The FeO/(FeO+MgO) ratio of tourmaline: a useful indicator of spatial variations in granite-related hydrothermal mineral deposits," *Journal of Geochemical Exploration*, vol. 42, no. 2-3, pp. 371–381, 1992.

[9] M. G. Kreĭn and F. È. Melik-Adamjan, "An integrated lithogeochemical approach to detecting and interpreting cryptic alteration around the Elura Zn-Pb-Ag deposit, New South Wales, Australia," *Geochemistry: Exploration, Environment, Analysis*, vol. 11, pp. 233–246, 2011.

[10] T. H. Pearce, "A contribution to the theory of variation diagrams," *Contributions to Mineralogy and Petrology*, vol. 19, no. 2, pp. 142–157, 1968.

[11] C. R. Stanley and H. E. Madeisky, "Lithogeochemical Exploration for Hydrothermal Ore Deposits Using Molar Element Ratio Analysis," in *Alteration and Alteration Processes Associated with Ore-Forming Systems: Short Course Notes*, D. R. Lentz, Ed., vol. 11, pp. 193–211, Geological Association of Canada, 1994.

[12] E. Urqueta, T. K. Kyser, A. H. Clark, C. R. Stanley, and C. J. Oates, "Lithogeochemistry of the Collahuasi porphyry Cu-Mo and epithermal Cu-Ag (-Au) cluster, northern Chile:

Pearce element ratio vectors to ore," *Geochemistry: Exploration, Environment, Analysis*, vol. 9, pp. 9–17, 2009.

[13] C. T. Barrie, "Petrochemistry of shoshonitic rocks associated with porphyry copper-gold deposits of central Quesnellia, British Columbia Canada," *Journal of Geochemical Exploration*, vol. 48, p. 258, 1993.

[14] J. Date, T. Watanabe, and Y. Saeki, "Zonal alteration around the Fukazawa kuroko deposits, Akita prefecture, northern Japan," *Economic Geology*, vol. 5, pp. 365–386, 1983.

[15] Y. Ishikawa, T. Sawaguchi, S. Iwaya, and M. Horiuchi, "Delineation of prospecting targets for Kuroko deposits based on modes of volcanism of underlying dacite and alteration haloes," *Mining Geology*, vol. 26, pp. 105–117, 1976.

[16] A. Kishida and R. Kerrich, "Hydrothermal alteration zoning and gold concentration at the Kerr–Addison Archean lode gold deposit, Kirkland Lake, Ontario," *Economic Geology*, vol. 82, no. 3, pp. 649–690, 1987.

[17] R. R. Large and P. J. Mcgoldrick, "Lithogeochemical halos and geochemical vectors to stratiform sediment hosted Zn-Pb-Ag deposits: part 2. HYC deposit, McArthur River, Northern Territory Queensland," *Journal of Geochemical Exploration*, vol. 68, no. 1-2, pp. 105–126, 2000.

[18] R. R. Large, J. McPhie, J. B. Gemmell, W. Herrmann, and G. J. Davidson, "The spectrum of ore deposit types, volcanic environments, alteration halos, and related exploration vectors in submarine volcanic successions: some examples from Australia," *Economic Geology*, vol. 96, no. 5, pp. 913–938, 2001.

[19] M. Piché and M. Jébrak, "Normative minerals and alteration indices developed for mineral exploration," *Journal of Geochemical Exploration*, vol. 82, no. 1-3, pp. 59–77, 2004.

[20] K. Prendergast, "Application of lithogeochemistry to gold exploration in the St Ives Goldfield, Western Australia," *Geochemistry: Exploration, Environment, Analysis*, vol. 7, pp. 99–108, 2007.

[21] L. Wang, J. Percival, J. W. Hedenquist, K. Hattori, and K. Z. Qin, "Alteration mineralogy of the Zhengguang Au-Zn deposit, Northeast China: interpretation of shortwave infrared analyses during mineral exploration and assessment," *Economic Geology*, vol. 116, no. 2, pp. 389–406, 2021.

[22] W. Zheng, Y. Chen, J. Tang et al., "Discovery of the tubular ore body in Jiama ore district, Tibet and its geological significance," *Mineral Deposits*, vol. 30, pp. 207–217, 2011.

[23] W. Zheng, J. Tang, K. Zhong et al., "Geology of the Jiama porphyry copper-polymetallic system, Lhasa Region, China," *Ore Geology Reviews*, vol. 74, pp. 151–169, 2016.

[24] B. Lin, J. Tang, P. Tang et al., "Polycentric complex mineralization model of porphyry system: a case study of Jiamasuperlarge deposit in Tibet," *Mineral Deposits*, vol. 38, pp. 1204–1222, 2019.

[25] Y. Y. Wang, W. B. Zheng, Y. C. Chen et al., "Discussion on the mechanism of seperation of copper and molybdenum in Jiama porphyry deposit system," *Acta Petrologica Sinica*, vol. 33, pp. 495–514, 2017.

[26] B. Zou, B. Lin, W. B. Zheng et al., "The characteristics of alteration and mineralization and geochronology of ore-bearing porphyry in south pit of Jiama copper-polymetallic deposit," *Tibet. Acta Petrologica Sinica*, vol. 35, pp. 953–967, 2019.

[27] J. Tang, L. Zhang, Y. Huang et al., "^{40}Ar /^{39}Ar isotope ages of main geological bodies in Xiongcun copper-gold deposit ,Xietongmen County , Tibet , and their geological significance," *Mineral deposit*, vol. 28, pp. 759–769, 2009.

[28] J. Tang, D. Wang, X. Wang, K. Zhong, L. Ying, and W. Zheng, "Geological features and metallogenic model of the Jiama copper-polymetallic deposit in Tibet," *Acta Geoscientia Sinica*, vol. 31, pp. 495–506, 2010.

[29] J. Tang, S. Deng, and W. Zheng, "An exploration model for Jiama copper polymetallic deposit in Maizhokunggar County, Tibet," *Mineral Deposits*, vol. 30, pp. 179–195, 2011.

[30] E. J. Hill, N. H. S. Oliver, J. S. Cleverley, M. J. Nugus, J. Carswell, and F. Clark, "Characterisation and 3D modelling of a nuggety, vein-hosted gold ore body, Sunrise Dam, Western Australia," *Journal of Structural Geology*, vol. 67, pp. 222–234, 2014.

[31] E. A. D. Kemp, T. Monecke, M. Sheshpari, E. Girard, and G. Bellefleur, "3D GIS as a support for mineral discovery," *Geochemistry: Exploration, Environment, Analysis*, vol. 11, pp. 117–128, 2011.

[32] S. H. H. Nielsen, F. Cunningham, R. Hay, G. Partington, and M. Stokes, "3D prospectivity modelling of orogenic gold in the Marymia Inlier, Western Australia," *Ore Geology Reviews*, vol. 71, pp. 578–591, 2015.

[33] G. Wang, S. Zhang, C. Yan et al., "Mineral potential targeting and resource assessment based on 3D geological modeling in Luanchuan region, China," *Computers & Geosciences*, vol. 37, no. 12, pp. 1976–1988, 2011.

[34] J. Chen, P. Lu, W. Wu, J. Zhao, and Q. Hu, "A 3-D prediction method for blind orebody based on 3-D visualization model and its application," *Earth Science Frontiers*, vol. 14, no. 5, pp. 54–61, 2007.

[35] K. Xiao, N. Li, A. Porwal, E. J. Holden, L. Bagas, and Y. Lu, "GIS-based 3D prospectivity mapping: a case study of Jiama copper-polymetallic deposit in Tibet, China," *Ore Geology Reviews*, vol. 71, pp. 611–632, 2015.

[36] A. Romero, C. Gatta, and G. Camps-Valls, "Unsupervised deep feature extraction for remote sensing image classification," *IEEE Transactions on Geoscience & Remote Sensing*, vol. 54, no. 3, pp. 1349–1362, 2016.

[37] J. Xia, N. Falco, J. A. Benediktsson, P. Du, and J. Chanussot, "Hyperspectral image classification with rotation random forest via KPCA," *IEEE Journal of Selected Topics in Applied Earth Observations & Remote Sensing*, vol. 10, pp. 1601–1609, 2017.

[38] B. Scholkopf, A. J. Smola, and K. R. Müller, "Nonlinear component analysis as a kernel eigenvalue problem," *Neural Computation*, vol. 10, no. 5, pp. 1299–1319, 1998.

[39] L. J. Cao, K. S. Chua, W. K. Chong, H. P. Lee, and Q. M. Gu, "A comparison of PCA, KPCA and ICA for dimensionality reduction in support vector machine," *Neurocomputing*, vol. 55, no. 1-2, pp. 321–336, 2003.

[40] C. Scheidt and J. Caers, "Representing spatial uncertainty using distances and kernels," *Mathematical Geoscience*, vol. 41, no. 4, pp. 397–419, 2009.

[41] Y. Gu, L. Ying, and Z. Ye, "A selective KPCA algorithm based on high-order statistics for anomaly detection in hyperspectral imagery," *IEEE Geoscience & Remote Sensing Letters*, vol. 5, no. 1, pp. 43–47, 2008.

[42] X. Ge, Y. Fan, X. Zhu, S. Deng, and Y. Wang, "A method to differentiate degree of volcanic reservoir fracture development using conventional well logging data—an application of kernel principal component analysis (KPCA) and multifractal detrended fluctuation analysis (MFDFA)," *IEEE Journal of Selected Topics in Applied Earth Observations & Remote Sensing*, vol. 7, pp. 4972–4978, 2015.

[43] E. J. M. Carranza and M. Hale, "Logistic regression for geologically constrained mapping of gold potential, Baguio district, Philippines," *Exploration and Mining Geology*, vol. 10, no. 3, pp. 165–175, 2001.

[44] A. Porwal, E. J. M. Carranza, and M. Hale, "Artificial neural networks for nineral-potential mapping: a case study from Aravalli Province Western India," *Natural resources research*, vol. 12, no. 3, pp. 155–171, 2003.

[45] R. Zuo and E. J. M. Carranza, "Support vector machine: a tool for mapping mineral prospectivity," *Computational Geosciences*, vol. 37, no. 12, pp. 1967–1975, 2011.

[46] R. Zuo, Y. Xiong, J. Wang, and E. J. M. Carranza, "Deep learning and its application in geochemical mapping," *Earth-Science Reviews*, vol. 192, pp. 1–14, 2019.

[47] T. Sun, H. Li, K. Wu, F. Chen, Z. Zhu, and Z. Hu, "Data-driven predictive modelling of mineral prospectivity using machine learning and deep learning methods: a case study from southern Jiangxi Province, China," *Minerals*, vol. 10, no. 2, p. 102, 2020.

[48] J. Xiang, K. Xiao, E. Carranza, J. Chen, and S. Li, "3D mineral Prospectivity mapping with random forests: a case study of Tongling, Anhui China," *Natural Resources Research*, vol. 29, pp. 1–20, 2019.

[49] B. Li, B. Liu, K. Guo, C. Li, and B. Wang, "Application of a maximum entropy model for mineral prospectivity maps," *Minerals*, vol. 9, no. 9, p. 556, 2019.

[50] B. Li, B. Liu, G. Wang, L. Chen, and K. Guo, "Using geostatistics and maximum entropy model to identify geochemical anomalies: a case study in Mila Mountain region, southern Tibet," *Applied Geochemistry*, vol. 124, p. 104843, 2021.

[51] S. J. Phillips, R. P. Anderson, and R. E. Schapire, "Maximum entropy modeling of species geographic distributions," *Ecological Modelling*, vol. 190, no. 3-4, pp. 231–259, 2006.

[52] S. J. Phillips and E. Jane, "On estimating probability of presence from use-availability or presence-background data," *Ecology*, vol. 94, no. 6, pp. 1409–1419, 2013.

[53] A. L. Berger, S. A. D. Pietra, and V. J. D. Pietra, "A maximum entropy approach to natural language processing," *Computational Linguistics*, vol. 22, pp. 39–71, 2002.

[54] Y. Dong, G. E. Hinton, N. Morgan, J. T. Chien, and S. Sagayama, "Introduction to the special section on deep learning for speech and language processing," *IEEE Transactions on Audio, Speech, and Language Processing*, vol. 20, pp. 4–6, 2012.

[55] Y. Xu, Z. Wu, J. Long, and X. Song, "A maximum entropy method for a robust portfolio problem," *Entropy*, vol. 16, no. 6, pp. 3401–3415, 2014.

[56] B. Wang, Y. Xu, and J. Ran, "Predicting suitable habitat of the Chinese monal (Lophophorus lhuysii) using ecological niche modeling in the Qionglai Mountains, China," *Peerj*, vol. 5, article e3477, 2017.

[57] N. Guo, C. Thomas, J. Tang, and Q. Tong, "Mapping white mica alteration associated with the Jiama porphyry-skarn Cu deposit, central Tibet using field SWIR spectrometry," *Ore Geology Reviews*, vol. 108, pp. 147–157, 2019.

[58] S. Chung, J. Ji, D. Liu, M. Chu, and Q. Zhang, "Adakites from continental collision zones: melting of thickened lower crust beneath southern Tibet," *Geology*, vol. 31, no. 11, pp. 1021–1024, 2003.

[59] Z. Hou, Z. Yang, X. Qu et al., "The Miocene Gangdese porphyry copper belt generated during post-collisional extension in the Tibetan Orogen," *Ore Geology Reviews*, vol. 36, no. 1-3, pp. 25–51, 2009.

[60] C. Miller, R. Schuster, U. Klötzli, W. Frank, and F. Purtscheller, "Post-collisional potassic and ultrapotassic magmatism in SW Tibet: geochemical and Sr–Nd–Pb–O isotopic constraints for mantle source characteristics and petrogenesis," *Journal of Petrology*, vol. 40, pp. 699–715, 1999.

[61] G. Pan, X. Mo, Z. Hou et al., "Spatial-temporal framework of the Gangdese Orogenic Belt and its evolution," *Acta Petrologica Sinica*, vol. 22, pp. 521–533, 2006.

[62] S. Turner, C. Hawkesworth, J. Liu, N. Rogers, S. Kelley, and C. P. Van, "Timing of Tibetan uplift constrained by analysis of volcanic rocks," *Nature*, vol. 364, no. 6432, pp. 50–54, 1993.

[63] K. Zhong, D. Yao, J. Duo et al., "Structural features of Yebatectonite group in Jiama(Gyama)- Qulong area of Tibet," *Acta Geoscientia Sinica*, vol. 34, pp. 75–86, 2013.

[64] Z. P. Qin, X. W. Wang, J. Dor, J. X. Tang, Y. Zhou, and H. J. Peng, "LA-ICP-MS U-Pb zircon age of intermediate–acidic intrusive rocks in Jiama of Tibet and its metallogenic significance," *Mineral Deposits*, vol. 30, pp. 339–349, 2011.

[65] W. P. Wang and J. X. Tang, "Rock types and genetic significance of hornfels and location prediction of concealed porphyry bodies in Jiama copper polymetallic deposit Tibet," *Mineral Deposits*, vol. 30, pp. 1017–1038, 2011.

[66] K. Zhong, L. Li, H. Zhou et al., "Features of Jiama(Gyama)-Kajunguo thrust-gliding nappe tectonic system in Tibet," *Acta Geoscientia Sinica*, vol. 33, pp. 411–423, 2012.

[67] B. Scholkopf, S. Mika, C. C. Burges et al., "Input space versus feature space in kernel-based methods," *IEEE Transactions on Neural Networks*, vol. 10, no. 5, pp. 1000–1017, 1999.

[68] J. Yang, A. F. Frangi, J. Y. Yang, D. D. Zhang, and Z. Jin, "KPCA plus LDA: a complete kernel fisher discriminant framework for feature extraction and recognition," *IEEE Transactions on Pattern Analysis and Machine Intelligence*, vol. 27, no. 2, pp. 230–244, 2005.

[69] M. Fauvel, J. Chanussot, and J. A. Benediktsson, "Kernel principal component analysis for the classification of hyperspectral remote sensing data over urban areas," *Eurasip Journal on Advances in Signal Processing*, vol. 2009, no. 1, 2009.

[70] C. E. Shannon, "A mathematical theory of communication," *Bell Labs Technical Journal*, vol. 27, no. 3, pp. 379–423, 1948.

[71] C. Ge, Z. Zhang, M. Kyebambe, and N. Kimbugwe, "Predicting the outcome of NBA playoffs based on the maximum entropy principle," *Entropy*, vol. 18, no. 12, p. 450, 2016.

[72] E. T. Jaynes, "Information theory and statistical mechanics," *Physical Review*, vol. 106, no. 4, pp. 620–630, 1957.

[73] D. Shepard, "A two-dimensional interpolation function for irregularly-spaced data," in *Proceedings of the 1968 23rd ACM national conference*, pp. 517–524, 1968.

[74] W. B. Zheng, *The Study on Metallogenic Model and Prospecting Pattern for Jiama Polymetallic Copper Deposit, Tibet, China*, CAGS, New York, 2012.